Check for updates

Zitierweise: *Angew. Chem. Int. Ed.* **2025**, *64*, e202412835
doi.org/10.1002/anie.202412835

CO_2 Hydrogenation Hot Paper

Manufacturing Single-Atom Alloy Catalysts for Selective CO_2 Hydrogenation via Refinement of Isolated-Alloy-Islands

Sibei Zou, Yuhang Liang, Xingmo Zhang, Qinfen Gu, Lizhuo Wang, Haoyue Sun, Xiaozhou Liao, Jun Huang,* and Assaad R. Masri*

Abstract: Single-atom alloy (SAA) catalysts exhibit huge potential in heterogeneous catalysis. Manufacturing SAAs requires complex and expensive synthesis methods to precisely control the atomic scale dispersion to form diluted alloys with less active sites and easy sintering of host metal, which is still in the early stages of development. Here, we address these limitations with a straightforward strategy from a brand-new perspective involving the 'islanding effect' for manufacturing SAAs without dilution: homogeneous RuNi alloys were continuously refined to highly dispersed alloy-islands (~1 nm) with completely single-atom sites where the relative metal loading was as high as 40 %. Characterized by advanced atomic-resolution techniques, single Ru atoms were bonded with Ni as SAAs with extraordinary long-term stability and no sintering of the host metal. The SAAs exhibited 100 % CO selectivity, over 55 times reverse water-gas shift (RWGS) rate than the alloys with Ru cluster sites, and over 3–4 times higher than SAAs by the dilution strategy. This study reports a one-step manufacturing strategy for SAA's using the wetness impregnation method with durable high atomic efficiency and holds promise for large-scale industrial applications.

[*] S. Zou, Prof. X. Liao, Prof. A. R. Masri
Department: School of Aerospace, Mechanical and Mechatronic Engineering
Institution: The University of Sydney
J07 The University of Sydney, New South Wales 2006, Australia
E-mail: szou4607@uni.sydney.edu.au

Y. Liang, X. Zhang, Dr. L. Wang, H. Sun, Prof. J. Huang
Department: School of Chemical and Biomolecular Engineering
Institution: The University of Sydney
J01 The University of Sydney, New South Wales 2006, Australia
E-mail: jun.huang@sydney.edu.au

Dr. Q. Gu
Institution: Australian Synchrotron
800 Blackburn Rd Clayton, Victoria, 3168, Australia

© 2024 The Authors. Angewandte Chemie published by Wiley-VCH GmbH. This is an open access article under the terms of the Creative Commons Attribution Non-Commercial NoDerivs License, which permits use and distribution in any medium, provided the original work is properly cited, the use is non-commercial and no modifications or adaptations are made.

Introduction

Single-atom alloy (SAA) catalysts have attracted much attention in the field of single-site catalysis in recent years because of their high reactivity, product selectivity, and excellent thermal stability.[1] To successfully synthesize SAA catalysts, previous strategies focused on first predicting the possible metal combinations through calculating the segregation energy and aggregation energy of metals [2] and then diluting the percentage of one metal to a very low level (< 3 at.%) in atomic dispersion in another bulk metal with highly precise methods like galvanic replacement or atomic layer deposition (ALD).[3] In this case, the SAA particle sizes are usually large (> 5 nm) to provide enough hosting agents for isolated active sites.[4] Even though the single-atom sites can be stabilized by the isolation of the host metal elements during highly thermal processes, the irreversible sintering of host metal still leads to deactivation with low long-term stability hence preventing SAAs from practical application.[4a,b] Besides, SAAs synthesized by complex and expensive methods still show low catalytic efficiency in product yield with low active metal loadings.[5] It is still challenging to synthesise high-dispersed SAAs with ultrafine sizes and sufficient active sites to overcome these limitations for large-scale application in industry.[6]

Coincidently, scientists have recently proposed a strategy to eliminate similar limitations in single-atom catalysts.[7] They tried to confine the single-atom on the high-dispersed metal-oxide supports with small size and isolated the metal-oxide supports with each other on another high-surface area inert support.[7] For example, Li et al. synthesized thermal-stable CeO_x with less than 2 nm size dispersed on high-surface area SiO_2 as the 'nanoglues' to anchor one Pt atom on each isolated CeO_x support island, where the single atoms can be isolated physically on the CeO_x without any agglomeration.[8] In another study, Hui et al.[9] anchored multiple isolated Pt atoms on gold quantum dots with narrow size distribution around 2.3 nm. The gold (111) quantum dots were grown epitaxially with Pt-Cl_4 single interfacial sites by the electrodeposition approach. These latest single-atom catalysis results (in 2022–2023) show that when the diameter of the nano-support is small enough (around 0.5–1 nm), isolated from each other, and thermally stable, the distribution of single atoms on the carrier is dense, and this could engender the outstanding catalytic performance.[7,10]

This inspiration can be extended from supported mono-metallic catalysts to alloys. When the alloyed nanoparticles

© 2024 The Authors. Angewandte Chemie published by Wiley-VCH GmbH

are small enough, the active metal with less amount will finally disperse as single atoms on each isolated nanoalloys as SAAs with enhancing active sites, where the relative metal loading can be as high as 40 wt % in our study (relative to the host metal). The uniform isolated alloyed nanoparticles act as 'islands', which can depart from each other and be refined as smaller ones. When the 'islands' are small enough, the single atoms can be self-restrained with host metal as SAAs on each isolated nano-alloys, like the 'islanding effect'. The success of this strategy requires the fulfilment of several major conditions: (1) a TiO_2 support that promoted the formation of homogeneous alloys, (2) controllable homogeneous alloy nanoparticle sizes, and (3) narrow size distribution.

The reverse water-gas shift (RWGS, $CO_2 + H_2 \rightarrow CO + H_2O$, $\Delta H_{298K} = 41\ kJ \bullet mol^{-1}$), one of the most significant selective CO_2 hydrogenation,[11] has attracted great interests since CO is a highly valuable feedstock to produce fuels and chemicals in Fischer–Tropsch synthesis.[12] However, the high CO selectivity is always accompanied by a significant decrease in CO_2 activity, especially at low temperatures since RWGS is an endothermic reaction.[11b,13] In our study, highly dispersed SAAs synthesized by the new strategy exhibited 100 % product selectivity to CO and extraordinary stability exceeding 140 hours, significantly improved the RWGS reaction performance and prevented the sintering of SAA nanoparticles as compared to the SAAs synthesised using traditional strategy.[4a]

Results and Discussion

Catalysts Structure Characterizations

A new strategy for synthesising SAAs as 'refinement for isolated-alloy-islands' without diluting metal loadings has been proposed by a series of RuNi bimetallic catalysts, as shown in Figure 1a. The homogeneous alloy particles (the combination of two metals in nanoparticles is random, without segregation or phase separation) can be refined to a point where the less abundant element is distributed as single atoms on each isolated alloy-island by adjusting the total amount of the metal precursors with a fixed metal atom ratio in the synthesis process. An extreme example of this strategy is that if the Ru/Ni atomic ratio is 1/4, there will inevitably be a Ru single atom on a highly dispersed cluster of 5 atoms. The single-atoms can be stable anchored on host metal as isolated-alloy-islands, which exhibit highly thermal stability without any aggregation of both single atoms and sintering of host metals after long-term stability test (over 140-h in our study). Additionally, the highly dispersed single-atom sites provide enough active sites for catalytic reaction, solving the disadvantage of SAA with low efficiency of active sites because of diluted alloy with low metal loadings. This strategy consists of the following three major conditions: (1) TiO_2 support that promotes homogeneous alloy formation and distribution, (2) the formation of homogeneous, stable, and isolated nanoalloy-islands (without segregation or agglomeration), (3) an easy-controlled method for the size of nanoalloy-islands that is general.

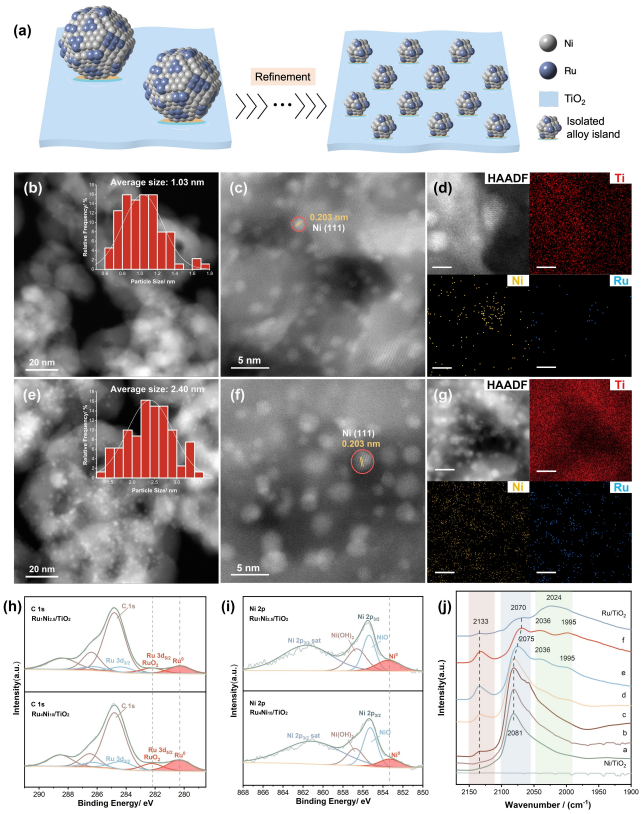


Figure 1. (a) Synthesis strategy Scheme of highly dispersed single atom alloys with abundant active sites—the refinement for isolated nano-alloy-islands. Basic catalytic structure characterizations: (b) a low-magnification STEM-HAADF image and the corresponding size distribution calculation of $Ru_1Ni_{2.5}/TiO_2$; (c) a high-magnification STEM-HAADF image and (d) the related EDS maps of nanoclusters in $Ru_1Ni_{2.5}/TiO_2$ (scale bars in EDS maps are 1 nm); (e) low-magnification STEM-HAADF and the corresponding size distribution calculation of Ru_4Ni_{10}/TiO_2; (f) high-magnification STEM-HAADF and (g) the related EDS maps of nanoclusters in Ru_4Ni_{10}/TiO_2 (scale bar in EDS images are 5 nm); (h) XPS results of C 1s in $Ru_1Ni_{2.5}/TiO_2$and Ru_4Ni_{10}/TiO_2; (i) XPS results of Ni 2p in $Ru_1Ni_{2.5}/TiO_2$ and Ru_4Ni_{10}/TiO_2; (j) CO-DRIFTS of all samples (a. $Ru_{0.5}Ni_{1.25}/TiO_2$, b. $Ru_1Ni_{2.5}/TiO_2$, c. Ru_2Ni_5/TiO_2, d. $Ru_3Ni_{7.5}/TiO_2$, e. Ru_4Ni_{10}/TiO_2, f. $Ru_5Ni_{12.5}/TiO_2$).

A series of RuNi bimetallic nanoalloy with particle sizes ranging from 0.9 to 3.9 nm were successfully synthesized with different metal loadings, where the average particle sizes were characterized by scanning transmission electron microscopy with high-angle annular dark-field (STEM-HAADF) (Figure 1 and S1–2). Both the bigger nanoalloy-islands (Ru_4Ni_{10}/TiO_2) and the smaller ones ($Ru_1Ni_{2.5}/TiO_2$) are dispersed evenly with narrow size distribution as 'nano-alloy-islands' on the TiO_2 supports, without any observation of particle aggregation in low-magnification of STEM-HAADF images (Figure 1b and 1e). In the high-magnification STEM-HAADF (Figure 1c and 1f), both the bigger nanoalloy-islands and the smaller ones exhibit uniform lattice fringes of approximately 0.203 nm, corresponding to Ni (111),[4c] indicating the Ni as the host-metal in the

© 2024 The Authors. Angewandte Chemie published by Wiley-VCH GmbH

15213757, 2025, 1, Downloaded from https://onlinelibrary.wiley.com/doi/10.1002/ange.202412835 by Ansto, Wiley Online Library on [03/07/2025]. See the Terms and Conditions (https://onlinelibrary.wiley.com/terms-and-conditions) on Wiley Online Library for rules of use; OA articles are governed by the applicable Creative Commons License

nanoalloy islands. Subsequently, the elemental distribution analysis conducted through energy dispersive spectroscopy (EDS) mappings (Figure 1d and 1g, S3–4) suggests that Ru is highly dispersed on the Ni host-metal particles, confirming the existence of RuNi alloy in both catalysts. In X-ray photoelectron spectroscopy (XPS) results (Figure 1h–i, S5), the binding energies of Ru^0 and Ni^0 in both catalysts show no shifts with similar proportions of Ru^0 and Ni^0 (in Table S2). This reveals that the bulk electron transfer between Ni and Ru and the overall reduction degree in the two catalysts shows no significant difference.

Infrared spectroscopy is a valuable technique for the in-depth characterization of the atomic coordination environment in catalysts.[14] The high resolution (2–4 cm^{-1}) provides unique fingerprints of active sites, allowing differentiation between very similar but different samples at atomic scale.[4b,15] All CO-diffuse reflectance infrared Fourier transform spectroscopy (CO-DRIFTS) spectra collected here are chemisorption *CO species on catalysts under Ar atmosphere without detection of gas phase CO (2100 and 2200 cm^{-1}).[15a,16] As shown in Figure 1j, only catalysts with Ru species remain existing chemisorption signal for CO under Ar. Ni species show very weak CO chemisorption[17] that desorb as soon as purging by Ar (in Figure S7). Therefore, there is no CO chemisorption peak on Ni/TiO_2 can be captured by DRIFTS when no gas phase of CO is detected (in Figs. S7 and 1j). Therefore, different *CO adsorption peaks in all bimetallic catalysts can be attributed to different Ru coordination environments. In previous research on CO-DRIFTS of Ru catalysts,[16a,18] the broad peak at the range of 2000–2040 cm^{-1} can be attributed to linear Ru-CO adsorption on high coordination Ru^0 sites. Meanwhile, the 2070–2081 cm^{-1} peak with another parallel accompanied peak at around 2130–2140 cm^{-1} is generally assigned as partially oxidized Ru^{n+} sites on monometallic Ru catalysts such as Ru/SiO_2 and Ru/Al_2O_3 (in Figure S8).[16a] The active site at a sole narrow peak of 2081 cm^{-1} without a parallel accompanied peak can be identified as the $Ru^{n+}(CO)_2$ adsorbed on low-coordinated isolated Ru sites surrounded by Ni in RuNi alloys. Based on this finding, the Ru single atom sites are present as dominate site in $Ru_{0.5}Ni_{1.25}$ and $Ru_1Ni_{2.5}$ catalysts (samples a-b) (Figure 1j, S9a). From Ru_2Ni_5 to $Ru_5Ni_{12.5}$ (samples c–f), the Ru cluster sites become dominate as the increasing intensity in linear adsorption site of Ru (2000–2040 cm^{-1}), with the pair of 2133 cm^{-1} and 2070–2075 cm^{-1} peaks being parallel (Figure 1j, S9b–d). The CO-DRIFTS experiments provide direct observation of Ru sites on RuNi nanoalloy-islands, confirming single-atom alloy formation in $Ru_{0.5}Ni_{1.25}$ and $Ru_1Ni_{2.5}$ catalysts.

The atomic resolution STEM-HAADF experiments are conducted on $Ru_1Ni_{2.5}/TiO_2$ and Ru_4Ni_{10}/TiO_2. In a typical STEM-HAADF image, the Ru atoms can be distinguished from Ni atoms due to the higher Z contrast of Ru, where the intensity of atoms is approximately proportional to the square root of atomic number.[14,19] Therefore, it has become a powerful tool to identify single atom sites and single atom alloys as an advanced atom-scale characterization in recent years.[1b,20] In Figure 2b, there is the significant brightest

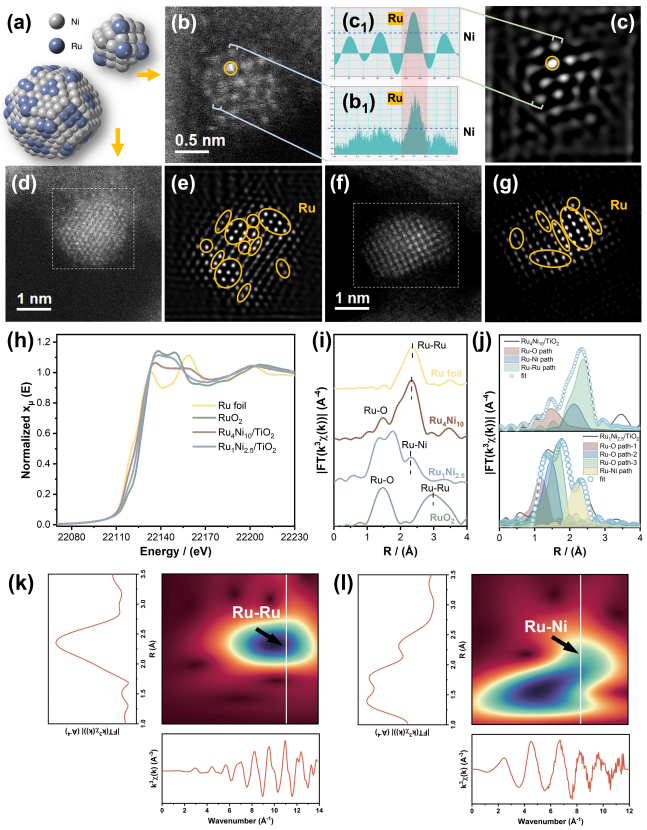


Figure 2. Identification of Ru single atom sites in the RuNi alloy: (a) schematic of the bimetallic nanocluster structure over $Ru_1Ni_{2.5}/TiO_2$ (top-right) and Ru_4Ni_{10}/TiO_2 (bottom-left); (b) an atomic-resolution STEM-HAADF image of a nanocluster in $Ru_1Ni_{2.5}/TiO_2$ and (b1) the corresponding line intensity profile of a row of atoms in the blue region; (c) The IFFT processed image of (b) and (c1) the corresponding line intensity profile of a row of atoms in the green region; (d) an atomic-resolution STEM-HAADF image of a nanoparticle in Ru_4Ni_{10}/TiO_2 and (e) the corresponding IFFT processed image; (f) an atomic-resolution STEM-HAADF image of another nanoparticle in Ru_4Ni_{10}/TiO_2 and (g) the corresponding IFFT processed image. (The yellow circles in the STEM-HAADF images highlight the Ru single-atom or Ru cluster sites on Ni.) (h) Ru K-edge XANES for $Ru_1Ni_{2.5}/TiO_2$, Ru_4Ni_{10}/TiO_2, a Ru foil, and RuO_2; (i) Ru K-edge EXAFS Fourier-transform spectra in R space; (j) the fitting results of EXAFS in R space of Ru_4Ni_{10}/TiO_2 and $Ru_1Ni_{2.5}/TiO_2$; and the k^3-weighted wavelet transform with Morlet Function for the Ru k-edge of (k) Ru foil and (l) $Ru_1Ni_{2.5}/TiO_2$. (The Ru foil and RuO_2 samples in the figures are standard samples as references.)

atom on a size of about 0.9 nm nanocluster, as compared to other atoms around. To better observe this phenomenon, the original image was then processed by inverse fast Fourier transform (IFFT), which obviously shows a brighter and bigger atom highlighted by a yellow circle, as shown in Figure 2c. Combine with line intensity distribution of a row of atoms in both original and IFFT images (in Figure $2b_1$–c_1), the individual Ru atom can be identified on Ni nanoclusters, confirming the formation of RuNi single atom alloy in $Ru_1Ni_{2.5}/TiO_2$ catalyst. On the other hand, for Ru_4Ni_{10}/TiO_2 catalyst, few of Ru single atom sites and most of cluster sites can be identified on Ni nanoparticles, as

© 2024 The Authors. Angewandte Chemie published by Wiley-VCH GmbH

15213757, 2025, 1, Downloaded from https://onlinelibrary.wiley.com/doi/10.1002/ange.202412835 by Ansto, Wiley Online Library on [03/07/2025]. See the Terms and Conditions (https://onlinelibrary.wiley.com/terms-and-conditions) on Wiley Online Library for rules of use; OA articles are governed by the applicable Creative Commons License

highlighted by yellow circles, with nanoalloy size of around 2.4 nm (in Figure 2d–g). This suggests Ru cluster sites on bigger nanoalloy-islands. The alloy nanoparticle with Ru cluster sites structure is also confirmed by the electron energy loss spectroscopy (EELS) analysis in Figure S10.

Ru K-edge and Ni K-edge X-ray adsorption spectra (XAS) experiments were further conducted to probe the local structure of the single atom Ru sites in smaller nanoalloy-islands. As shown in Figure 2h, the normalized Ru K-edge X-ray absorption near-edge structures (XANES) spectra of two catalysts indicates that both the average valence states of Ru in $Ru_1Ni_{2.5}/TiO_2$ and Ru_4Ni_{10}/TiO_2 are between Ru foil and RuO_2, indicating partial oxidation of the alloy surface under ex-situ conditions. The Ru K-edge features of Ru_4Ni_{10}/TiO_2 are similar to the ones of the Ru foil reference, confirming the presence of Ru cluster sites in the alloyed structure. On the other hand, the Ru K-edge features of $Ru_1Ni_{2.5}/TiO_2$ show significant differences between Ru_4Ni_{10}/TiO_2 and Ru foil reference, indicating no Ru metallic structures. From the further analysis of Ni K-edge XANES spectra (in Figure S11), similar Ni K-edge features to Ni foil of both $Ru_1Ni_{2.5}/TiO_2$ and Ru_4Ni_{10}/TiO_2 are shown except for the intensity, confirming the major presence of metallic Ni nanoparticles but with different coordination environment of Ru species in RuNi alloyed structure.

Fourier-transformed k^3-weighted extended X-ray adsorption fine structure (EXAFS) in R space of catalysts are analysed to clarify the coordination environment of Ru atoms in Ni nanoparticles.[4d,21] In the second shell corresponding to the metallic coordination environment (in Figure 2i–j), there is only Ru–Ni (2.31 Å) scattering path in $Ru_1Ni_{2.5}/TiO_2$ while there are both Ru–Ni (2.31 Å) and Ru–Ru (2.35 Å) scattering paths in Ru_4Ni_{10}/TiO_2. It is worth noting that the Ru–Ni coordination number in $Ru_1Ni_{2.5}/TiO_2$ from the R-space fitting results (in Table S3) is 0.54, which is much lower than the one in Ru_4Ni_{10}/TiO_2 (1.48). This result indicates that in smaller nanoalloy-islands Ru atoms tends to occupy low coordination sites such as the surface exposed corner or edge sites. This has been revealed by the previous theoretical calculation studies.[22] The R-space fitting results in Ru K-edge are also consistent with the CO-DRIFTS (Figure 2i), where the low-coordination Ru site gradually becomes dominant as the decrease of alloyed nanoparticle sizes. In the k^3-weighted wavelet transform (WT) analysis [23] of the Ru K-edge EXAFS (in Figure 2k–l and S12), the metallic Ru–Ru bond should be the maximum wave signal at ~11.0 $Å^{-1}$ in K-space according to Ru foil, while the Ru–O bond and Ru–Ru bond in RuO_2 should be at ~7.0 $Å^{-1}$ and ~9.0 $Å^{-1}$, respectively. However, the metallic bonds in $Ru_1Ni_{2.5}/TiO_2$ show the maximum wave signal at 8.5 $Å^{-1}$, confirming the no Ru–Ru metallic bonds (in Figure 2l). The metallic bonds in Ru_4Ni_{10}/TiO_2 show the maximum wave signal at ~8.5 $Å^{-1}$ as Ru–Ni bonds and ~11.0 $Å^{-1}$ as Ru–Ru bonds (in Figure S12). The EXAFS and the atomic-resolution STEM-HAADF results of $Ru_1Ni_{2.5}/TiO_2$ and Ru_4Ni_{10}/TiO_2 catalysts are highly consistent, confirming the single Ru atom site with Ru–Ni scattering in $Ru_1Ni_{2.5}/TiO_2$ and the cluster Ru site with Ru–Ni and Ru–Ru scatterings in Ru_4Ni_{10}/TiO_2.

Catalytic Performance and Stability

To understand the trend of catalytic performance as the active sites change of RuNi nanoalloy islands, the product selectivity for CO_2 hydrogenation is further evaluated on all catalysts under 400 °C, which is the window temperature for both RWGS and CO_2 methanation. Over 99 % of CO selectivity is on the smaller nanoalloy-islands but gradually switches to CH_4 on the bigger ones (Figure 3a and S13). The smaller nanoalloy-islands with single Ru atom sites leading to extremely high CO selectivity while the bigger ones with Ru cluster sites leading to decreasing CO selectivity as shown in the schematic (Figure 3b). Moreover, the CO_2 conversion to CO rate per gram RuNi catalysts shows a significant drop from 1.0 to 2.4 nm while remains unchanged over 2.4 nm (Figure 3c). The CO_2 conversion rate reaches the highest with the bimetallic particle sizes of 1.0 nm, which is the size of single atom alloy formation.

The catalytic performance for CO_2 hydrogenation under different temperatures is further evaluated on smaller nanoalloy-islands with single Ru atom sites ($Ru_1Ni_{2.5}/TiO_2$) and bigger nanoalloy-islands with Ru cluster sites (Ru_4Ni_{10}/TiO_2). In Figure 3d, the $Ru_1Ni_{2.5}/TiO_2$ exhibit an overall higher CO_2 conversion rate than Ru_4Ni_{10}/TiO_2 and 100 % selectivity of CO under all temperatures. At lower temperatures under 375 °C, the Ru_4Ni_{10}/TiO_2 shows a slightly higher CO_2 conversion rate but with little increase as the temperature increases. However, different from Ru_4Ni_{10}/TiO_2, the $Ru_1Ni_{2.5}/TiO_2$ shows lower rate at lower temperatures but with a significant increase of CO_2 conversion rate as the temperature increase. The different tendency in reaction rate indicates different CO_2 activation routes on two catalysts. At the same time, the CO selectivity on Ru_4Ni_{10}/TiO_2 start to increase only after 450 °C while the one on $Ru_1Ni_{2.5}/TiO_2$ remains 100 % CO selectivity under all temperatures. The formation of RuNi single atom alloy shows extraordinary efficiency in improving both the CO_2 hydrogenation performance and CO product selectivity, even at lower temperatures.

To further clarify the role of SAA structure and particle size effect in enhancing RWGS performance, a series of Ru_xNi_{10}/TiO_2 (x = metal loading of Ru, x = 0.5,1,2,4) catalysts with fixed Ni loading are evaluated as comparison. With lowering the Ru contents in alloy nanoparticles, the SAA structure in diluted alloy nanoparticles is confirmed by the STEM-HAADF (in Figure S14). This is the conventional SAA synthesis strategy. Only the alloy catalysts with SAA structures (Ru_1Ni_{10}/TiO_2 and $Ru_{0.5}Ni_{10}/TiO_2$) exhibit 100 % CO selectivity (in Figure S15). Since the nanoparticle size of Ru_1Ni_{10}/TiO_2 and Ru_4Ni_{10}/TiO_2 is similar and characterized by XRD and STEM-HAADF (in Figure S16), it can confirm that only the SAA structure plays key roles in the high CO selectivity despite the particle size. In addition, the high-dispersed SAA catalysts exhibit a 3–4 times higher CO formation rate than the conventional SAA catalysts with diluted active metal sites (in Figure 3e). As compared to other reported efficient catalysts for RWGS (in Table S4), the $Ru_1Ni_{2.5}/TiO_2$ catalysts show even higher CO formation rate than Pt-based catalysts. This result further evidence the

© 2024 The Authors. Angewandte Chemie published by Wiley-VCH GmbH

15213757, 2025, 1, Downloaded from https://onlinelibrary.wiley.com/doi/10.1002/ange.202412835 by Ansto, Wiley Online Library on [03/07/2025]. See the Terms and Conditions (https://onlinelibrary.wiley.com/terms-and-conditions) on Wiley Online Library for rules of use; OA articles are governed by the applicable Creative Commons License

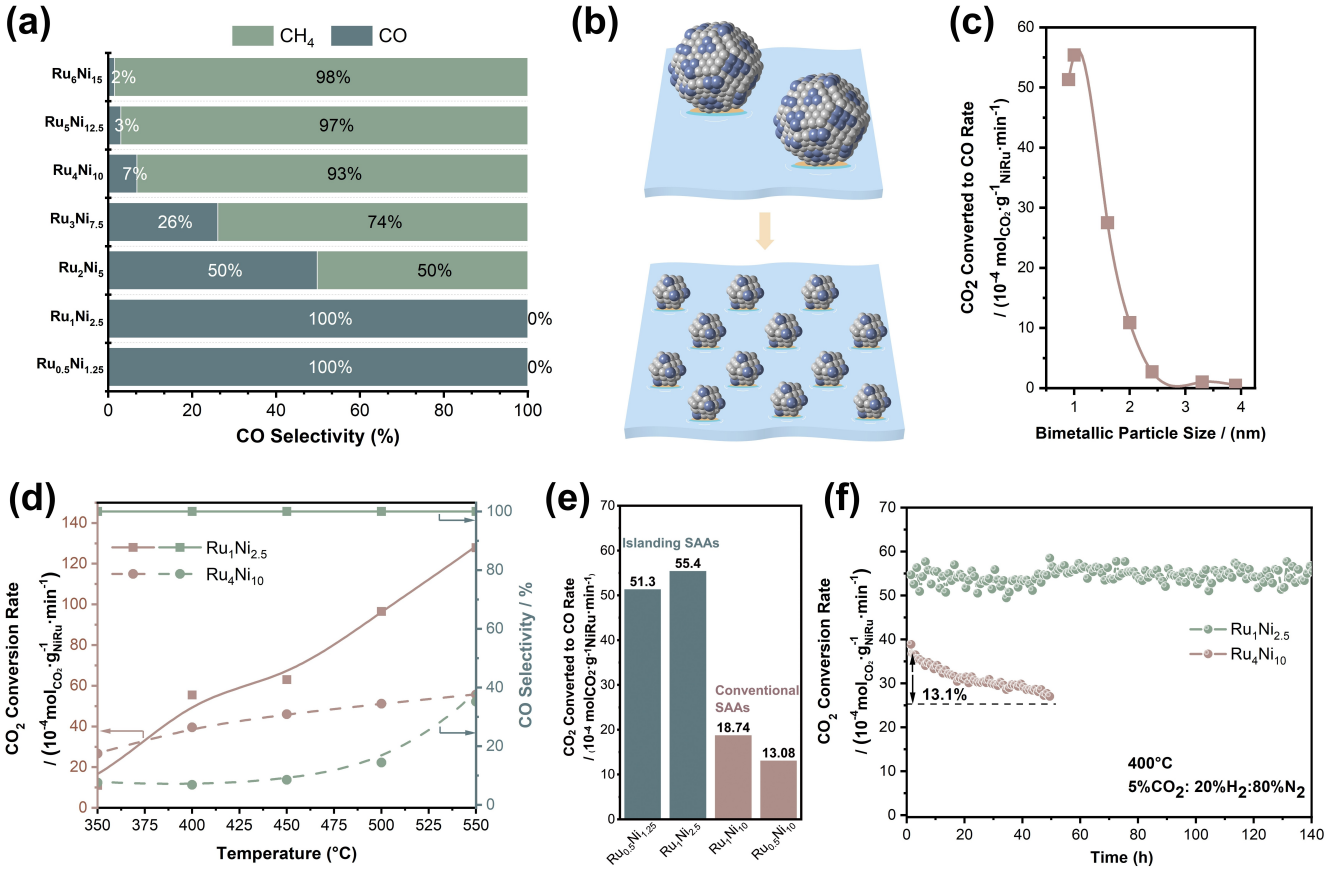


Figure 3. (a) Product selectivity over different catalysts at 400 °C; (b) the scheme of nanoalloy island isolation with different active sites leading to different product selectivity; (c) RWGS rate over catalysts with different bimetallic average particle size at 400 °C; (d) CO_2 conversion and product selectivity over $Ru_1Ni_{2.5}/TiO_2$ and Ru_4Ni_{10}/TiO_2 catalysts from 350 to 550 °C; (e) RWGS rate over catalysts with single-atom alloy structure by the islanding effect strategy compared with the ones by conventional diluted alloy strategy; (f) the long-term stability tests on $Ru_1Ni_{2.5}/TiO_2$ and Ru_4Ni_{10}/TiO_2 catalysts at 400 °C.

advanced performance RWGS reaction of SAA catalysts synthesized by the islanding strategy proposed in this work.

In the field of heterogeneous catalysis, the thermal stability of catalysts lays the foundation for their industrial applications and serves as a critical evaluation criterion for catalytic performance. As shown in Figure 3f, the bigger nanoalloy-islands with cluster Ru sites exhibits a certain decline of both activity and selectivity in long-term test. However, the smaller nanoalloy-islands with single atom sites show extraordinary thermal stability at 400 °C for over 140 h, indicating no change of active sites during the long-term stability test. The XRD results of $Ru_1Ni_{2.5}/TiO_2$ before and after 140 h reaction reveal that the catalyst maintains a similar structure to the fresh catalyst without agglomeration of single atoms because of no observation of metallic Ni or Ru diffraction peaks (Figure S17). In addition, the fresh and 140 h-spent catalysts particle distribution calculated by STEM-HAADF (Figure S17), the 140 h-spent catalysts show no significant change in the average size, further evidence of no agglomerated large nanoparticles. According to the STEM-HAADF and XRD results (in Figure S18), the decrease of the activity in Ru_4Ni_{10}/TiO_2 catalyst with bigger nanoalloy-islands can be attributed to the structural destruction of alloy particles into ones with smaller size. Previous studies on SAAs have already demonstrated their outstanding thermal stability, which overcomes the challenge of sintering in single-atom site catalysts.[2b,4b,24] However, it was observed that Cu host nanoparticles got sintering after heating catalysts to 600 °C but still with Pt isolated single atom sites in PtCu SAA catalysts.[4b] The host metal nanoparticle sintering limits the performance of SAAs. Excitingly, the SAAs synthesised by refinement nanoalloy-islands strategy in this work not only retain the stability of single-atom Ru site with extraordinary activity and selectivity stability, but also overcome the limitation of sintering in the host metal particles.

Catalytic Mechanism Studies

To comprehensively elucidate the mechanism how the highly dispersed SAAs significantly improve the performance of the RWGS reaction, a series of in situ DRIFTS characterization experiments are designed for $Ru_1Ni_{2.5}/TiO_2$ and Ru_4Ni_{10}/TiO_2. For the CO_2 hydrogenation, the activation process of CO_2 is the most challenging step due to the

© 2024 The Authors. Angewandte Chemie published by Wiley-VCH GmbH

15213757, 2025, 1, Downloaded from https://onlinelibrary.wiley.com/doi/10.1002/ange.202412835 by Ansto, Wiley Online Library on [03/07/2025]. See the Terms and Conditions (https://onlinelibrary.wiley.com/terms-and-conditions) on Wiley Online Library for rules of use; OA articles are governed by the applicable Creative Commons License

stability of CO_2 molecular structure, which remains controversial in mechanism study with the complex intermediate species.[25] The CO_2 temperature-programmed dissociation without H_2 on monometallic catalysts (Ni/TiO_2 and Ru/TiO_2) and pure TiO_2 support are firstly observed with in situ DRIFTS (Figure S19) to elucidate the active sites for CO_2 activation. The CO_2 is firstly adsorbed on TiO_2 support. However, the CO_2 can only directly dissociate to *CO on Ru/TiO_2, indicating Ru is the active sites for CO_2 direct dissociation to *CO species binding on Ru metals. There are three configurations of CO_2 adsorption on TiO_2 (Figure S20), including *HCO_3 (bicarbonate, 1673–1647 cm^{-1}, 1434–1401 cm^{-1}), *CO_3 (carbonate, 1521–1460 cm^{-1}, 1389–1356 cm^{-1}), and *CO_2 (carboxylate, 1350–1341 cm^{-1}).[16b,26] While intermediates during the dissociation procedure are *HCO_2 (formate, 1557–1553 cm^{-1}, 1455–1430 cm^{-1}, 2876 cm^{-1}, and 2956 cm^{-1}) on TiO_2 and *CO (low coordination:2075–2064 cm^{-1} and high coordination: 2012–2004 cm^{-1}) on Ru in NiRu alloys.[27]

Steady-state in situ DRIFTS experiments at different temperatures under reaction conditions on two catalysts are analysed in detail to reveal the reaction route. As shown in Figure 4a–b, the adsorption behaviour of intermediates including *HCO_3, *CO_3, *CO_2, *HCO_2, and *CO are different on two catalysts, indicating different reaction routes. As for the $Ru_1Ni_{2.5}/TiO_2$ catalyst (Figure 4a), CO_2 is firstly absorbed as *HCO_3 and *CO_2 species and can hardly dissociate to *CO or *HCO_2 at 60 °C on $Ru_1Ni_{2.5}/TiO_2$. But the generation of *CO species is accelerated from 150 to 250 °C simultaneously with the red shift of *HCO_2 peak

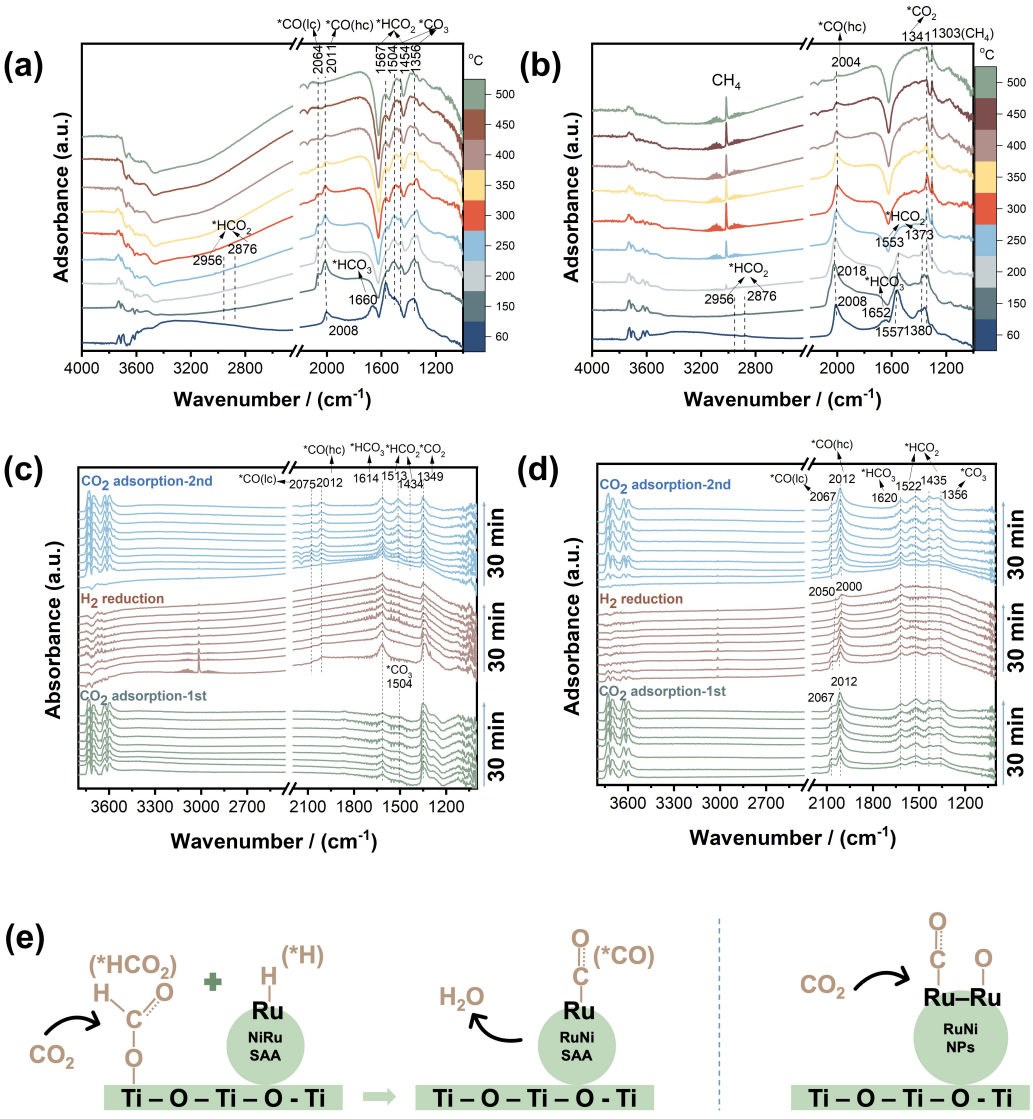


Figure 4. Steady-state in situ DRIFTS experiments are conducted under the reaction conditions under the feed gas mixture (CO_2/H_2 = 1/4, balanced with N_2, total flow rate 60 sccm) flow at the temperature range from 60 to 500 °C: (a) $Ru_1Ni_{2.5}/TiO_2$ catalysts; (b) Ru_4Ni_{10}/TiO_2 catalysts. Transition-state in situ DRIFTS experiments are conducted by alternatively switching the adsorption gas three times to first 5 % CO_2 in N_2, then 20 % H_2 in N_2, and finally 5 % CO_2 in N_2 again on (c) $Ru_1Ni_{2.5}/TiO_2$ under 350 °C and (d) Ru_4Ni_{10}/TiO_2 at 250 °C, which are the starting temperature of the reaction on two catalysts. (e) The different CO_2 activation routes on $Ru_1Ni_{2.5}/TiO_2$ and Ru_4Ni_{10}/TiO_2.

© 2024 The Authors. Angewandte Chemie published by Wiley-VCH GmbH

15213757, 2025, 1, Downloaded from https://onlinelibrary.wiley.com/doi/10.1002/ange.202412835 by Ansto, Wiley Online Library on [03/07/2025]. See the Terms and Conditions (https://onlinelibrary.wiley.com/terms-and-conditions) on Wiley Online Library for rules of use; OA articles are governed by the applicable Creative Commons License

from 1560 to 1556 cm^{-1} (Figure 4a and S21b). It suggests that the generation of *CO species on $Ru_1Ni_{2.5}/TiO_2$ is mainly hydrogenated from $*HCO_2$.[11b] *CO species rapidly desorb as CO gas without further hydrogenation.

On the other hand, the *CO species can be observed immediately on Ru_4Ni_{10}/TiO_2 as introducing the reaction gases at 60 °C, indicating CO_2 directly dissociate to *CO and $*HCO_2$ (Figure 4b). The $*HCO_2$ can also hydrogenated with a red shift from 1557 to 1553 cm^{-1} (Figure S22b). Rather than desorption as CO gas, *CO species are further hydrogenated to CH_4 with a red shift from 2018 to 2004 cm^{-1}. The rate limitation steps on Ru_4Ni_{10}/TiO_2 is the further hydrogenation of *CO species, since *CO species are the only intermediate can be captured by DRIFTS during the reaction process. The reaction rate of Ru_4Ni_{10}/TiO_2 is higher than $Ru_1Ni_{2.5}/TiO_2$ at lower temperatures (below 375 °C) but significantly lower than $Ru_1Ni_{2.5}/TiO_2$ as increasing temperature (in Figure 3d) with the rate limitation of *CO hydrogenation to CH_4 on Ru_4Ni_{10}/TiO_2.

The different Ru sites on two catalyst play vital roles in both CO_2 activation routes and product selectivity. Then the transition-state in situ DRIFTS analysis at the initial temperature of the catalytic reaction on two catalysts are conducted. As shown in Figure 4c–d, the CO_2 can rapidly dissociate to *CO on Ru_4Ni_{10}/TiO_2 even without H_2 introduction, which is the same as on Ru/TiO_2. In contrast, no appearance of *CO species on $Ru_1Ni_{2.5}/TiO_2$ without H_2. Additionally, the second CO_2 adsorption behaviours of two catalysts after H_2 introduction show significant difference. The generation of *CO species can be observed as soon as the CO_2 introduction with the appearance of $*HCO_2$ on $Ru_1Ni_{2.5}/TiO_2$ while there shows no change in CO_2 activation on Ru_4Ni_{10}/TiO_2 as compared to the first round of CO_2 adsorption. This result can also be confirmed by the CO_2 temperature programmed desorption (CO_2-TPD) and temperature-programmed surface reaction (TPSR) experiments (Figure S23). The $*HCO_2$ species on $Ru_1Ni_{2.5}/TiO_2$ can be generated during the CO_2-TPD under Ar. In addition, consumption peaks related to OH groups are observed at the IR range of 3500–3800 cm^{-1}[28] as $*HCO_2$ formation on $Ru_1Ni_{2.5}/TiO_2$, confirming the reaction route that CO_2 first is activated with the OH group on TiO_2 support. However, $*HCO_2$ species accumulate with increasing temperature without introducing H_2 while dissociating to *CO as soon as with abundant *H species. This result indicates that the CO_2 cannot dissociate on $Ru_1Ni_{2.5}/TiO_2$ without H_2. At the same time, there are no consumption peaks related to OH groups when *CO species formation on Ru_4Ni_{10}/TiO_2. This result further proves that activation sites for CO_2 direct dissociation to *CO species are Ru cluster sites on alloy rather than the OH group on TiO_2 in Ru_4Ni_{10}/TiO_2.

For the CO_2 direct dissociation, it is necessary to involve at least two Ru sites as illustrated in the schematic (Figure 4e). Therefore, it should hardly take place on single Ru atom sites. For the CO_2 dissociation with H_2 through $*HCO_2$, the $*HCO_2$ can easily dissociate on the single Ru atom sites, as illustrated in the schematic. Therefore, the CO_2 dissociation to *CO can be significantly facilitated after H_2 introduction. According to previous research, the energy barrier of CO_2 direct dissociation route is lower than that of through $*HCO_2$ route, which results in a higher reaction rate at lower temperatures on Ru_4Ni_{10}/TiO_2.[29] Combined with the steady-state and transition-state in situ DRIFTS experiments, it can be evidenced that the activation site and reaction site on $Ru_1Ni_{2.5}/TiO_2$ are separated, where the CO_2 is first activated on TiO_2 support and further hydrogenated to CO on Ru single atom sites. However, both the activation site and reaction site are Ru cluster sites on Ru_4Ni_{10}/TiO_2. Therefore, the separated dual sites on $Ru_1Ni_{2.5}/TiO_2$ break the linear scaling relationship,[12a] which significantly facilitate the catalytic reaction rates. The possible reaction routes on $Ru_1Ni_{2.5}/TiO_2$ can be unravelled as follows:

$$\boldsymbol{CO_2 + Ti - OH \rightarrow Ti - HCO_3}$$

$$\boldsymbol{Ti - HCO_3 + H^* \rightarrow Ti - COOH + O^*}$$

$$Ti - COOH + H^* \rightarrow Ru - CO + H_2O$$

$$M - CO + 2H^* \rightarrow CO\ (g) + M - OH$$

The possible reaction routes on Ru_4Ni_{10}/TiO_2 can be unravelled as follows:

$$\boldsymbol{CO_2 \rightarrow Ru - CO + Ru - O}$$

$$\boldsymbol{Ru - CO + H^* \rightarrow Ru - CH + Ru - O}$$

$$Ru - CH + 3H^* \rightarrow Ru - CH_4$$

$$Ru - CH_4 \rightarrow CH_4\ (g)$$

Notably, as soon as the hydrogen is introduced, a substantial amount of methane is generated on $Ru_1Ni_{2.5}/TiO_2$ under the excess hydrogen environment, contrary to the expected product selectivity. This phenomenon firstly suggests that *CO adsorbed on $Ru_1Ni_{2.5}/TiO_2$ is highly unstable. Secondly, it implies that the hydrogen dissociation ability of $Ru_1Ni_{2.5}/TiO_2$ is comparable to that of Ru_4Ni_{10}/TiO_2. Therefore, the *CO adsorption behaviour on two catalysts is vital for product selectivity.

To unravel the mechanisms of different product selectivity on catalysts with different active sites, the desorption behaviours of *CO species with and without H_2 on two catalysts at different temperatures are observed with in situ DRIFTS (Figure 5a–d). The results demonstrate that the desorption rate of *CO on $Ru_1Ni_{2.5}/TiO_2$ surpasses that on Ru_4Ni_{10}/TiO_2 with the increasing temperature (Figure 5a and 5c). It is worth noting that, even in the presence of hydrogen, *CO species cannot be further hydrogenated but rather accelerates the desorption process on $Ru_1Ni_{2.5}/TiO_2$, where notable *CO desorption can be observed at 50 °C (Figure 5b). On the contrary, *CO species are further hydrogenated to CH_4 on Ru_4Ni_{10}/TiO_2 (Figure 5d). Combined with the identification of active sites in two catalysts (Figure 1–2), it can be concluded that the single atom Ru sites on $Ru_1Ni_{2.5}/TiO_2$ are mainly bound to the low coordination *CO species, which are less stable than the

© 2024 The Authors. Angewandte Chemie published by Wiley-VCH GmbH

15213757, 2025, 1, Downloaded from https://onlinelibrary.wiley.com/doi/10.1002/ange.202412835 by Ansto, Wiley Online Library on [03/07/2025]. See the Terms and Conditions (https://onlinelibrary.wiley.com/terms-and-conditions) on Wiley Online Library for rules of use; OA articles are governed by the applicable Creative Commons License

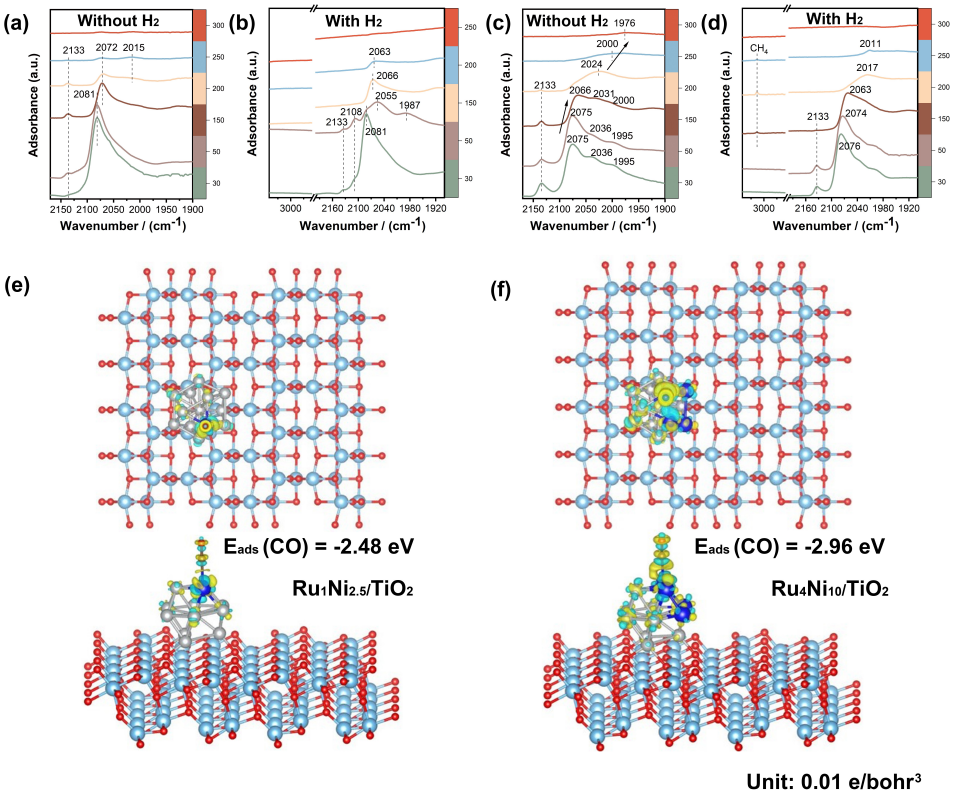


Figure 5. *CO species desorption in situ DRIFTS of $Ru_1Ni_{2.5}/TiO_2$ at different temperatures: (a) without H_2 and (b) dissociate with 5% H_2 in N_2. *CO species desorption in situ DRIFTS of Ru_4Ni_{10}/TiO_2 at different temperatures: (c) without H_2 and (d) dissociate with 5% H_2 in N_2. The charge density differences of the *CO adsorbed on the atom-top site on (e) Ru cluster site and (f) Ru single atom alloy site on Ni (111) plane, where electrons are relocated from the yellow to the blue regions.

linear adsorption ones, promoting CO desorption and suppressing dissociation.[30] However, the Ru cluster sites on Ru_4Ni_{10}/TiO_2 facilitates the linear *CO adsorption, which is relatively stable and trends to be further dissociated to generate CH_4 with H_2.

Density functional theory (DFT) calculations are employed to study the electron density differences between single atom Ru sites and cluster Ru sites. It is assumed that the Ru cluster and single atom sites are on the alloyed Ni nanoparticle supported on TiO_2 (101) facet (in Figure S24). As shown in Figure S25, the electron transfer density redistribution indicates a significantly higher degree of localized electron transfer from Ni to Ru on Ru cluster sites than on the single atom sites. Subsequently, the adsorption energies of *CO on two kinds of Ru sites are calculated by DFT (in Figure 5e–f). Combined with the actual *CO adsorption sites observed by the in situ CO-DRIFTS (in Figure 1i), all catalysts exhibit strong adsorption at the range from 1950–2080 cm^{-1}, which are the top-atom sites and can be the representative active sites on catalysts in our work [31] (in Figure S26). The adsorption energy of *CO in SAA is −2.48 eV (Figure 5e). In comparison, adsorption energy of *CO on Ru cluster site is −2.96 eV / (Figure 5f). The top-atom sites on the SAAs show lower CO adsorption energies than the top-atom sites on the catalysts with Ru clusters. In conclusion, the Ru cluster sites lead to a stronger localized electron transfer between Ni and Ru, increasing the electron density in the Ru d-band. This enhanced the electron back-donation from Ru to absorbed *CO species, strengthening the Ru–C bond while weakening the C–O bond, facilitating the further hydrogenation of *CO to CH_4. In contrast, the relatively weaker localized electron redistribution on Ru single atom site weakens the electron back donation from Ru to *CO, which weakens the Ru–C bond while strengthens the C–O bond, leading to CO product selectivity with lower *CO adsorption energy.

Conclusion

In summary, a new strategy for synthesizing highly dispersed, ultrafine SAAs is proposed through refining the homogeneous RuNi nanoalloy-islands. A series of RuNi alloys (0.9–3.9 nm) with fixed metal ratio are constructed, where the SAAs can successfully form under with sizes around 1 nm. Assisted by the advanced high time-space resolution techniques, including STEM-HAADF with double spherical aberration corrected, in situ DRIFTS probed by CO molecules, and EXAFS, Ru single-atom sites can be observed on sizes of 0.9 to 1.0 nm alloyed nanoclusters while Ru cluster sites are on 1.6 to 3.9 nm alloyed nanoparticles. In each refined RuNi SAAs isolated island, the Ru atoms bonding with Ni, forming alloyed structure exhibit extraordinary thermal stability without sintering even after a 140-h

© 2024 The Authors. Angewandte Chemie published by Wiley-VCH GmbH

15213757, 2025, 1, Downloaded from https://onlinelibrary.wiley.com/doi/10.1002/ange.202412835 by Ansto, Wiley Online Library on [03/07/2025]. See the Terms and Conditions (https://onlinelibrary.wiley.com/terms-and-conditions) on Wiley Online Library for rules of use; OA articles are governed by the applicable Creative Commons License

long-term stability test. In addition, RuNi SAAs by islanding strategy exhibit 3–4 times higher CO formation rate than SAAs by the conventional strategy. Combined with in situ DRIFTS and DFT calculations, the separated CO_2 activation route and different electron properties of single atom Ru lead to higher CO_2 conversion rate and weaker adsorption energy of *CO, respectively, which is the key to enhancing the RWGS performance. This work provides new insights into synthesising high-dispersed and ultrafine SAAs with 'islanding effect' strategy. This significantly breaks the limitations of irreversible sintering of host-metal and low atomic efficiency with low metal loading in previous SAAs synthesis strategies.

Supporting Information

The authors have included experiment methods, supplementary Figures, and tables in the Supporting Information.

Acknowledgements

The author is supported by a scholarship from the University of Sydney, under the Sydney Nano CO_2Zero Grand Challenge Program. This work is also supported by the funding from Australia Research Council Discovery Project (DP22002851 ARC).

The authors acknowledge the technical and scientific assistance of ***Sydney Microscopy & Microanalysis***, the University of Sydney node of Microscopy Australia. We acknowledge the support provided by the ***Sydney Analytical*** at the University of Sydney with the XRD and XPS techniques. And we also acknowledge the technical and scientific support provided by the ***Australian Synchrotron*** for the XAS characterizations.

Australia Research Council Discovery Project (DP22002851 ARC) Open Access publishing facilitated by The University of Sydney, as part of the Wiley - The University of Sydney agreement via the Council of Australian University Librarians.

Conflict of Interest

The authors declare no conflict of interest.

Data Availability Statement

Research data are not shared.

Keywords: Single-atom alloys · CO_2 hydrogenation · Bimetallic catalysts · IR Spectroscopy · Electron Microscopy

[1] a) M. Ouyang, K. G. Papanikolaou, A. Boubnov, A. S. Hoffman, G. Giannakakis, S. R. Bare, M. Stamatakis, M. Flytzani-Stephanopoulos, E. C. H. Sykes, *Nat. Commun.* **2021**, *12*, 1549; b) G. Giannakakis, M. Flytzani-Stephanopoulos, E. C. H. Sykes, *Acc. Chem. Res.* **2019**, *52*, 237–247; c) M. T. Darby, M. Stamatakis, A. Michaelides, E. C. H. Sykes, *J. Phys. Chem. Lett.* **2018**, *9*, 5636–5646.

[2] a) Q. Fu, Y. Luo, *J. Phys. Chem. C* **2013**, *117*, 14618–14624; b) M. T. Darby, E. C. H. Sykes, A. Michaelides, M. Stamatakis, *Top. Catal.* **2018**, *61*, 428–438; c) H. L. Skriver, N. M. Rosengaard, *Phys. Rev. B* **1992**, *46*, 7157–7168.

[3] a) G. A. Somorjai, J. Carrazza, *Ind. Eng. Chem. Fundam.* **1986**, *25*, 63–69; b) R. A. Van Santen, *Acc. Chem. Res.* **2009**, *42*, 57–66.

[4] a) M. D. Marcinkowski, M. T. Darby, J. Liu, J. M. Wimble, F. R. Lucci, S. Lee, A. Michaelides, M. Flytzani-Stephanopoulos, M. Stamatakis, E. C. H. Sykes, *Nat. Chem.* **2018**, *10*, 325–332; b) G. Sun, Z.-J. Zhao, R. Mu, S. Zha, L. Li, S. Chen, K. Zang, J. Luo, Z. Li, S. C. Purdy, A. J. Kropf, J. T. Miller, L. Zeng, J. Gong, *Nat. Commun.* **2018**, *9*, 4454; c) W. Liu, H. Feng, Y. Yang, Y. Niu, L. Wang, P. Yin, S. Hong, B. Zhang, X. Zhang, M. Wei, *Nat. Commun.* **2022**, *13*, 3188; d) J. Zhao, J. Liu, Z. Li, K. Wang, R. Shi, P. Wang, Q. Wang, G. I. N. Waterhouse, X. Wen, T. Zhang, *Nat. Commun.* **2023**, *14*, 1909.

[5] L. Liu, A. Corma, *Chem. Rev.* **2023**, *123*, 4855–4933.

[6] T. Zhang, A. G. Walsh, J. Yu, P. Zhang, *Chem. Soc. Rev.* **2021**, *50*, 569–588.

[7] Z. Li, B. Li, Q. Li, *Adv. Mater.* **2023**, *35*, 2211103.

[8] X. Li, X. I. Pereira-Hernández, Y. Chen, J. Xu, J. Zhao, C.-W. Pao, C.-Y. Fang, J. Zeng, Y. Wang, B. C. Gates, J. Liu, *Nature* **2022**, *611*, 284–288.

[9] L. Hui, X. Zhang, Y. Xue, X. Chen, Y. Fang, C. Xing, Y. Liu, X. Zheng, Y. Du, C. Zhang, F. He, Y. Li, *J. Am. Chem. Soc.* **2022**, *144*, 1921–1928.

[10] a) B.-B. Xu, X.-B. Fu, X.-M. You, E. Zhao, F.-F. Li, Z. Chen, Y.-X. Li, X. L. Wang, Y.-F. Yao, *ACS Catal.* **2022**, *12*, 6958–6967; b) C. Ye, M. Zheng, Z. Li, Q. Fan, H. Ma, X. Fu, D. Wang, J. Wang, Y. Li, *Angew. Chem. Int. Ed.* **2022**, *61*, e202213366.

[11] a) S. Li, Y. Xu, Y. Chen, W. Li, L. Lin, M. Li, Y. Deng, X. Wang, B. Ge, C. Yang, S. Yao, J. Xie, Y. Li, X. Liu, D. Ma, *Angew. Chem. Int. Ed.* **2017**, *56*, 10761–10765; b) J. Zhang, S. Deo, M. J. Janik, J. W. Medlin, *J. Am. Chem. Soc.* **2020**, *142*, 5184–5193.

[12] a) Y. Wang, J. Chen, L. Chen, Y. Li, *ACS Catal.* **2023**, *13*, 3735–3742; b) Y. Wang, W. Zhan, Z. Chen, J. Chen, X. Li, Y. Li, *ACS Catal.* **2020**, *10*, 7177–7187.

[13] a) J. Wang, C.-Y. Liu, T. P. Senftle, J. Zhu, G. Zhang, X. Guo, C. Song, *ACS Catal.* **2020**, *10*, 3264–3273; b) M. D. Porosoff, B. Yan, J. G. Chen, *Energy Environ. Sci.* **2016**, *9*, 62–73.

[14] R. T. Hannagan, G. Giannakakis, M. Flytzani-Stephanopoulos, E. C. H. Sykes, *Chem. Rev.* **2020**, *120*, 12044–12088.

[15] a) J. C. Matsubu, V. N. Yang, P. Christopher, *J. Am. Chem. Soc.* **2015**, *137*, 3076–3084; b) D. A. Patel, R. T. Hannagan, P. L. Kress, A. C. Schilling, V. Çınar, E. C. H. Sykes, *J. Phys. Chem. C* **2019**, *123*, 28142–28147; c) R. Liu, J. N. El Berch, S. House, S. W. Meil, G. Mpourmpakis, M. D. Porosoff, *ACS Catal.* **2023**, *13*, 2449–2461.

[16] a) S. Y. Chin, C. T. Williams, M. D. Amiridis, *J. Phys. Chem. B* **2006**, *110*, 871–882; b) J. Zhou, Z. Gao, G. Xiang, T. Zhai, Z. Liu, W. Zhao, X. Liang, L. Wang, *Nat. Commun.* **2022**, *13*, 327.

[17] M. Xu, S. He, H. Chen, G. Cui, L. Zheng, B. Wang, M. Wei, *ACS Catal.* **2017**, *7*, 7600–7609.

[18] B. T. Loveless, C. Buda, M. Neurock, E. Iglesia, *J. Am. Chem. Soc.* **2013**, *135*, 6107–6121.

© 2024 The Authors. Angewandte Chemie published by Wiley-VCH GmbH

15213757, 2025, 1, Downloaded from https://onlinelibrary.wiley.com/doi/10.1002/ange.202412835 by Ansto, Wiley Online Library on [03/07/2025]. See the Terms and Conditions (https://onlinelibrary.wiley.com/terms-and-conditions) on Wiley Online Library for rules of use; OA articles are governed by the applicable Creative Commons License

[19] E. J. Peterson, A. T. DeLaRiva, S. Lin, R. S. Johnson, H. Guo, J. T. Miller, J. Hun Kwak, C. H. F. Peden, B. Kiefer, L. F. Allard, F. H. Ribeiro, A. K. Datye, *Nat. Commun.* **2014**, *5*, 4885.
[20] a) L. Zhang, R. Si, H. Liu, N. Chen, Q. Wang, K. Adair, Z. Wang, J. Chen, Z. Song, J. Li, M. N. Banis, R. Li, T.-K. Sham, M. Gu, L.-M. Liu, G. A. Botton, X. Sun, *Nat. Commun.* **2019**, *10*, 4936; b) M. Inazu, Y. Akada, T. Imaoka, Y. Hayashi, C. Takashima, H. Nakai, K. Yamamoto, *Nat. Commun.* **2022**, *13*, 2968.
[21] a) Z. Wang, C. Dong, X. Tang, X. Qin, X. Liu, M. Peng, Y. Xu, C. Song, J. Zhang, X. Liang, S. Dai, D. Ma, *Nat. Commun.* **2022**, *13*, 4404; b) P. Li, M. Wang, X. Duan, L. Zheng, X. Cheng, Y. Zhang, Y. Kuang, Y. Li, Q. Ma, Z. Feng, W. Liu, X. Sun, *Nat. Commun.* **2019**, *10*, 1711.
[22] a) H. Lee, Z.-H. Liao, P.-W. Hsu, T.-C. Hung, Y.-C. Wu, Y. Lin, J.-H. Wang, M.-F. Luo, *J. Chem. Phys.* **2017**, *147*, 044704; b) G. F. Zhao, Z. Zeng, *J. Chem. Phys.* **2006**, *125*, 014303.
[23] H. Funke, A. C. Scheinost, M. Chukalina, *Phys. Rev. B* **2005**, *71*, 094110.
[24] S. Ji, Y. Chen, X. Wang, Z. Zhang, D. Wang, Y. Li, *Chem. Rev.* **2020**, *120*, 11900–11955.
[25] a) K. Jalama, *Catal. Rev.* **2017**, *59*, 95–164; b) J. Ashok, S. Pati, P. Hongmanorom, Z. Tianxi, C. Junmei, S. Kawi, *Catal. Today* **2020**, *356*, 471–489; c) Y. Wang, L. R. Winter, J. G. Chen, B. Yan, *Green Chem.* **2021**, *23*, 249–267.
[26] a) L. Falbo, C. G. Visconti, L. Lietti, J. Szanyi, *Appl. Catal. B* **2019**, *256*, 117791; b) M. Inoue, K. Miyazaki, B. Lu, C. Song, Y. Honda, M. Arao, T. Ohwaki, M. Matsumoto, H. Imai, A. Shima, Y. Sone, R. C. Peng, T. Shibayanagi, T. Abe, *J. Phys. Chem. C* **2020**, *124*, 10016–10025; c) C. Wang, Y. Lu, Y. Zhang, H. Fu, S. Sun, F. Li, Z. Duan, Z. Liu, C. Wu, Y. Wang, H. Sun, Z. Yan, *Nano Res.* **2023**; d) M. González-Castaño, J. González-Arias, L. F. Bobadilla, E. Ruíz-López, J. A. Odriozola, H. Arellano-García, *Fuel* **2023**, *338*, 127241.
[27] S. Zou, L. Wang, H. Wang, X. Zhang, H. Sun, X. Liao, J. Huang, A. Masri, *Energy & Environmental Science* **2023**.
[28] a) K. P. Reddy, D. Kim, S. Hong, K.-J. Kim, R. Ryoo, J. Y. Park, *ACS Appl. Mater. Interfaces* **2023**, *15*, 9373–9381; b) M. Xu, S. Yao, D. Rao, Y. Niu, N. Liu, M. Peng, P. Zhai, Y. Man, L. Zheng, B. Wang, B. Zhang, D. Ma, M. Wei, *J. Am. Chem. Soc.* **2018**, *140*, 11241–11251; c) X. Xu, L. Liu, Y. Tong, X. Fang, J. Xu, D.-e. Jiang, X. Wang, *ACS Catal.* **2021**, *11*, 5762–5775.
[29] S. Piccinin, M. Stamatakis, *ACS Catal.* **2014**, *4*, 2143–2152.
[30] X. Chen, X. Su, H.-Y. Su, X. Liu, S. Miao, Y. Zhao, K. Sun, Y. Huang, T. Zhang, *ACS Catal.* **2017**, *7*, 4613–4620.
[31] J. Hulva, M. Meier, R. Bliem, Z. Jakub, F. Kraushofer, M. Schmid, U. Diebold, C. Franchini, G. S. Parkinson, *Science* **2021**, *371*, 375–379.

Manuscript received: July 8, 2024
Accepted manuscript online: August 22, 2024
Version of record online: October 25, 2024

© 2024 The Authors. Angewandte Chemie published by Wiley-VCH GmbH

15213757, 2025, 1, Downloaded from https://onlinelibrary.wiley.com/doi/10.1002/ange.202412835 by Ansto, Wiley Online Library on [03/07/2025]. See the Terms and Conditions (https://onlinelibrary.wiley.com/terms-and-conditions) on Wiley Online Library for rules of use; OA articles are governed by the applicable Creative Commons License